

Multi-Channel Implantable Cubic Rectenna MIMO System With CP Diversity in Orthogonal Space for Enhanced Wireless Power Transfer in Biotelemetry

Original

Multi-Channel Implantable Cubic Rectenna MIMO System With CP Diversity in Orthogonal Space for Enhanced Wireless Power Transfer in Biotelemetry / Kaim, Vikrant; Singh, Neeta; Kumar Kanaujia, Binod; Matekovits, Ladislau; Esselle, Karu P.; Rambabu, Karumudi. - In: IEEE TRANSACTIONS ON ANTENNAS AND PROPAGATION. - ISSN 0018-926X. - STAMPA. - 71:1(2023), pp. 200-214. [10.1109/TAP.2022.3222695]

Availability:

This version is available at: 11583/2974791 since: 2023-01-19T09:44:02Z

Publisher:

IEEE

Published

DOI:10.1109/TAP.2022.3222695

Terms of use:

This article is made available under terms and conditions as specified in the corresponding bibliographic description in the repository

Publisher copyright

IEEE postprint/Author's Accepted Manuscript

©2023 IEEE. Personal use of this material is permitted. Permission from IEEE must be obtained for all other uses, in any current or future media, including reprinting/republishing this material for advertising or promotional purposes, creating new collecting works, for resale or lists, or reuse of any copyrighted component of this work in other works.

(Article begins on next page)

Multi-Channel Implantable Cubic Rectenna MIMO System with CP Diversity in Orthogonal Space for Enhanced Wireless Power Transfer in Biotelemetry

Vikrant Kaim, *Member, IEEE*, Neeta Singh, *Member, IEEE*, Binod Kumar Kanaujia, *Senior Member, IEEE*, Ladislau Matekovits, *Senior Member, IEEE*, Karu P. Esselle, *IEEE Fellow*, and Karumudi Rambabu, *Member, IEEE*

Abstract— For wireless power transfer (WPT), an implantable cubic rectenna MIMO system (CRMS), operating in dual ISM frequency bands of 2.45 and 5.8 GHz, is presented as a receiver (R_x). CRMS is evolved to the proposed biocompatible full package cubic rectenna (FPCR) by including the power and data management circuit modules. The dual frequency bands differentiated by orthogonal circular polarization (CP) in a spatial quadrature would serve as propagation channels for power, data, and control signals. Four dual branch rectifiers are designed using both distributed and lumped elements on the backside of individual antenna elements. To demonstrate the feasibility of the proposed work as an integrated system for WPT, the structures are fabricated individually, where the transmitter (T_x), which is an external antenna, and rectifiers are tested in free space, and FPCR in a custom made canonical phantom. After validation of individual measurements, power delivery from the T_x to the FPCR is conducted experimentally to measure the integrated system's RF-DC total conversion efficiency (TCE). The FPCR is designed to receive low RF power (P_{RF}) of 0 dBm, where a single cubic rectenna element (CRE) provides DC power (P_{DC}) of 0.26 mW and 0.33 mW at 2.45 GHz and 5.8 GHz, respectively. Thereafter, the interconnection of CREs in a series/parallel configuration improved P_{DC} to 0.5/1.39 mW and 0.51/1.64 mW, respectively. Additionally, human safety is considered by evaluating a maximum permissible exposure (MPE) limit and specific absorption rate (SAR) distribution in a canonical tissue model when both T_x and FPCR are excited with 1W power.

Index Terms— Cubic rectenna MIMO system (CRMS), DC combiner, far-field WPT, multi-channel, polarization diversity, series-parallel connection, spatial diversity, specific absorption rate.

I. INTRODUCTION

Implantable medical devices (IMDs) have become ubiquitous in recent times. Such devices are useful in disease prevention,

health monitoring, and drug delivery [1]. The typical method of powering most of the devices is to use lithium batteries [2], but the in-built batteries of these devices pose a limitation for the long period of implantation [3] as these batteries have a finite operational cycle and need to be replaced frequently through invasive surgical operation[4]. Hence, the long term sustainable wireless powering of the IMDs has become crucial [5], [6], [7].

Different research groups have made their efforts to design the WPT system for biomedical applications. Progressively year-wise, in [8], far-field WPT is demonstrated using a multilayer antenna at 433 MHz. In [9], wireless powering is achieved using a phase-locked loop through an inductive link at 5 MHz. In [10], far-field WPT is achieved using an implantable rectenna (rectifier + antenna) with a PIFA antenna at 2.45 GHz. In [11], far-field WPT is demonstrated using a microstrip ring disk antenna at 2.45 GHz. In [5], non-leaky midfield WPT is obtained at 1.5 GHz using a conformal T-shaped ground slot antenna and near-field plates. In [12], a high efficiency magnetic resonant WPT system is designed using implantable flexible coils at 6.78 MHz. In [13], a near-field inductive link is demonstrated to power an implantable 3D millimeter size non-planar antenna at 402 MHz. In [3], WPT based on the magnetic resonant coupling is discussed based on spiral coils at 39.86 MHz. In [2], a radiating near-field patch rectenna is designed to transfer power wirelessly at 2.4 GHz. In [6], a metamaterial coupled WPT system based on cubic dielectric resonators is demonstrated at 447.1 MHz. In [14], a 50 Ω miniaturized rectenna is designed for wireless energy harvesting using spiral PIFA with circular polarization (CP) at 673 MHz. In [15], an arm-implantable rectenna is designed and supported by a PIFA antenna for far-field WPT at 915 MHz. In [16], an efficient midfield WPT system is demonstrated using a spiral wideband antenna at 1470 MHz. In [7], radiative near-field WPT is demonstrated using a meander line radiator at 1900 MHz. In [17], a WPT system is designed using split resonant rings and

(Corresponding author: Binod Kumar Kanaujia and Ladislau Matekovits)

V. Kaim and B. K. Kanaujia are with the School of Computational and Integrative Sciences, Jawaharlal Nehru University, New Delhi-110067, India, and B. K. Kanaujia is also with the Dr. B.R. Ambedkar National Institute of Technology, Jalandhar (Punjab)-144011, India (e-mail: vikran16_sit@jnu.ac.in, bkkanaujia@ieee.org).

Neeta Singh is with the Department of Electronics and Communication Engineering, Jamia Millia Islamia, New Delhi-110025, India (email: neeta.singh90@gmail.com).

L. Matekovits is with the Department of Electronics and Telecommunications, Politecnico di Torino, 10129 Turin, Italy, Istituto di

Elettronica e di Ingegneria dell'Informazione e delle Telecomunicazioni, National Research Council of Italy, 10129 Turin, Italy, and Politecnica University Timișoara, 300006 Timișoara, Romania (e-mail: ladislau.matekovits@polito.it).

K. P. Esselle is with the School of Electrical and Data Engineering, University of Technology Sydney, Ultimo, NSW, Australia (e-mail: Karu.Esselle@uts.edu.au).

K. Rambabu is with the Department of Electrical and Computer Engineering, University of Alberta, Edmonton, Alberta-T6G 2V4, Canada (e-mail: rambabu@ualberta.ca).

integrated with a miniaturized metasurface to enhance the WPT efficiency at 430 MHz. In [18], an efficient WPT system is designed in the radiative near-field region using a metamaterial-based CP slot antenna at 2.45 GHz. In [19], wireless powering of biomedical implants is demonstrated in the midfield region using a rectifier integrated self-diplexing implantable antenna at 1470 MHz.

Further, in modern wireless biomedical applications of sensing wandering patterns and freezing of gait detection in patients who have dementia and Parkinson's disease [20], [21], where the human body moves arbitrarily in urban or indoor environments [22], non line-of-sight (NLOS) communication between the T_x and the R_x is inevitable. Reflections and diffractions of the signal generate multiple polarization diverse signals with possible fading at the R_x side. Therefore, for wireless transmission of RF power, implantable multi-input-multi-output (MIMO) rectennas with polarization diversified capability are preferred [23] to augment the multipath reflections. Moreover, it could also ensure restriction-free mobility for the patients.

In literature, considerable number of WPT systems have already been proposed for different biomedical applications, but for most rectenna designs [2], [3], [5], [6], [7], [8]-[13], [15]-[17], [19], [24] linearly polarized (LP) antennas are adopted. This arrangement is problematic in practice since the polarization of the incident wave may vary from time to time due to the urban environment, and the collected power will fluctuate due to the polarization mismatch [23]. Such WPT systems suffer from lateral and angular misalignments between the transmitting (T_x) and receiving (R_x) antennas. To overcome the issues of LP systems and short range power transfer distances in the near-field region, it is essentially required to design a CP antenna based WPT system in the far-field region. However, only a few rectenna designs in [14], [18], and [25] have tried to explore CP rectennas for biomedical applications. For rectenna designs based on dual CP antennas, any LP incident waves and either RHCP or LHCP incident waves can be received. To conclude, previously, most of the researchers working in the biomedical engineering domain focussed on single implantable rectenna design, but, to carry out the function of multidirectional WPT for the multitasking IMDs, exploration of non-planar rectenna MIMO is desired. The concept of compact cubic MIMO antenna was pioneered by B.N. Getu and J.B. Andersen [26] for an indoor scattering environment where space, polarization, and pattern diversities could be fully exploited [22], [27], [28].

In this paper, CP implantable cubic rectenna MIMO system (CRMS) is designed as a R_x (see Fig. 1) to receive the incoming RF signals from the 360° environment with orthogonal circular polarizations in both 2.45 and 5.8 GHz ISM bands. The R_x is implanted in a canonical tissue phantom model of the human arm at a distance $X \geq 2D^2/\lambda$ (D is the largest antenna dimension, and λ is the corresponding wavelength in the air at operating frequency) from the T_x .

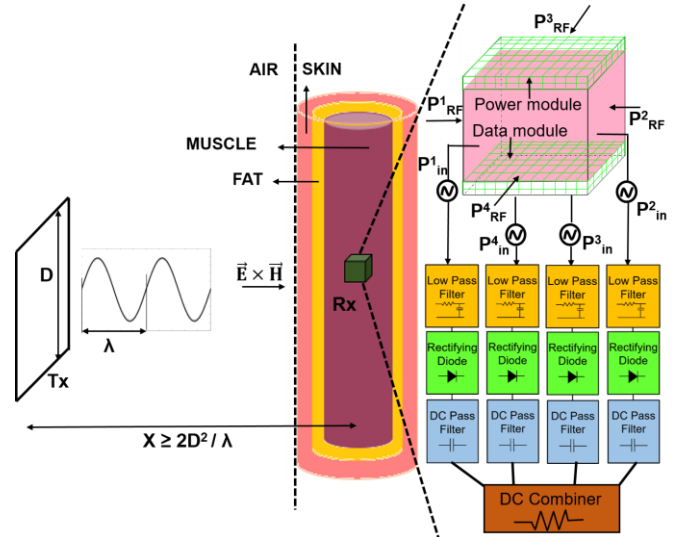


Fig. 1 WPT system of the proposed cubic rectenna MIMO system.

The received ambient power (P^i_{RF}) by the antenna elements in the tissue generates input power P^i_{in} ($i = 1, 2, 3, 4$), across the i^{th} rectifier port to be used by the active components of the circuit modules. The RF power from the LOS/NLOS directions is rectified separately through each CRE, and subsequently, the individual output DC power is combined in a series and parallel configuration. Finally, the performance of the FPCR is verified by comparing the simulated and measured results. Noted in this article, a symmetrical dual branch implantable rectifier circuit is designed to achieve small footprints with comparable DC power and conversion efficiency for low input powers at both 2.45 and 5.8 GHz resonant frequencies. A detailed comparison of the proposed WPT system with the existing systems is presented in Table I. Based on the comparison, the proposed rectenna topology is the only novel candidate that could harvest RF energy at a deep implantation site by receiving signals from multiple directions in a 4π steradian range [22], irrespective of the CP sense of an incident signal. It would also result in improved conversion efficiency as CP MIMO rectenna could produce stable DC power at random polarization angles [29]. Furthermore, in the counterparts, received power by the implantable antenna is enhanced using additional components such as lenses with a parasitic ring, matching layer, parasitic patch, near-field plate, or on-body antenna over the phantom [10], [11], [13], [5], [30], [31]. But, these methods could cause discomfort to the patient and restrict mobility, so a feasible and cost-effective method (DC combiner) is desired for power improvement. Therefore, for the first time, WPT is enhanced by using a DC combining circuit in this study. Note that we have not used an RF power combiner.

This paper consists of six sections, organized as follows. Section-I presents the introduction. Section-II presents the synthesis of multi-channel FPCR, dual-branch rectifier, and characterization of the external transmitter antenna. Section-III presents the simulated results of the proposed FPCR. Section-IV discusses the measured results of the rectifier, FPCR, and CRE, followed by power enhancement using a DC combiner. Section-V explores human safety from radiation by evaluating the maximum permissible exposure (MPE) limit and SAR distribution, followed by the concluding remarks in Section-VI.

Table I
COMPARISON OF THE PROPOSED WPT SYSTEM VERSUS REPORTED SYSTEM IN LITERATURE

References (Year)		[10] (2014)	[5] (2017)	[25] (2018)	[2] (2018)	[15] (2019)	[14] (2019)	[16] (2020)	[7] (2020)	[18] (2020)	[19] (2021)	Proposed (2022)
Rectenna Results	Freq. (GHz)	2.45 (ISM)	1.5 (Midfield)	0.915 (ISM)	2.4 (ISM)	0.915 (ISM)	0.673 (UHF)	1.47 (Midfield)	1.9 (non-ISM)	2.45 (ISM)	1.47 (Midfield)	2.45/5.8 (ISM)
	WPT Type	Far-Field	Midfield	Far-Field	Nearfield Radiative	Far-Field	Far-Field	Midfield	Nearfield Radiative	Nearfield Radiative	Midfield	Far-Field
	Transfer Distance	500 mm	65 mm	400 mm	420 mm	500 mm	500 mm	50 mm	20 mm	40 mm	60 mm	500 mm
	Tx (P_T) Power	24.3 dBm	30 dBm	25 dBm	16.5 dBm	25 dBm	10 dBm	30 dBm	30 dBm	30 dBm	30 dBm	30 dBm
	Rx (P_{RF}) Power	-24 dBm	-0.97 dBm	-22.89 dBm	0.79 dBm	-10 dBm	-41.15 dBm	8.26 dBm	3.97 dBm	0.26 dBm	10.29 dBm	-21/-8.6 dBm
	Simulation	Voxel Body	Heart Phantom	Skin Phantom	Free Space	Muscle Phantom	Multilayer Phantom	Muscle Phantom	Skin Phantom	Skin Phantom	Skin Phantom	Arm Phantom
	TCE(%)	0.0015	0.473	—	2.7	0.0058	—	0.67	0.25	—	1.07	0.14/0.16
	Power Enhance	Parasitic Patch	Nearfield Plate	NA	NA	Matching Layer	NA	Matching Layer	NA	MTM Slab	Matching Layer	DC Combine
	SAR (W/Kg)	0.145 (1-g)	410 (1-g)	—	—	—	0.078 (1-g)	0.187 (1-g)	—	9.627 (1-g)	0.17 (1-g)	0.0004/0.17 (1-g)
Rectifier	Type	One-Diode	—	One-Diode	Voltage Doubler	One-Diode	One-Diode	Voltage Doubler	Voltage Doubler	NA	One-Diode	One-Diode
	η (%)	42@ -10 dBm	—	44@ -10 dBm	48@ 10 dBm	43@ -10 dBm	40@ -20 dBm	90@ 2 dBm	82@ 2 dBm	NA	76.1@ 2 dBm	70@ -15 dBm
	Assembly	Antenna Separated	—	Antenna Separated	Antenna Integrated	Antenna Separated	Antenna Integrated	Antenna Separated	Antenna Separated	NA	Antenna Integrated	Antenna Integrate
External Antenna	Type	Horn Antenna	Pattern Patch	Patch	Patch Array	Log-Periodic	Log-Periodic	Slotted Patch	Spiral Coil	Patch	Slotted Patch	Patch
	Size (cm ²)	—	6.3 × 6.3	—	34 × 33	—	—	6 × 6	5 × 5	120 × 120	5 × 5	5 × 5
	Gain	7.6 dBi	—	8.0 dB	19 dBi	—	6.6 dB	—	—	2.51 dBi	—	4.2/3.4 dBic
Implantable Antenna Integrated Device	Freq. Bands	Single	Tri	Single	Single	Single	Single	Quad	Dual	Single	Dual	Dual
	Antenna Type	Patch	Patch	Patch	Patch	PIFA	Spiral PIFA	Meander Patch	Meander Patch	Slotted Patch	Slotted Patch	Cubic MIMO
	Antenna Profile	Planar	Conformal	Planar	Planar	Planar	Non-Planar	Planar	Planar	Planar	Planar	Non-Planar
	Volume (mm ³)	8×4×1.9	D=10.25, H=20.5	13×13×1.27	27.5×19.8×1.5	16×14×1.9	D=10, H=3.2	D=8, H=18	8.9×6.9×4.5	12.02×12.02×0.24	D=10, H=18	15×15×15
	Imp BW (%)	4.1	—	3.82	—	5.7	—	—	27.9	74.1	7.34	32.65/23.33
	Polarization	Linear Polarized	Linear Polarized	Circular Polarized	Linear Polarized	Linear Polarized	Circular Polarized	Linear Polarized	Linear Polarized	Circular Polarized	Linear Polarized	Circular Polarized
	Gain	-19 dBi	-34.6 dBi	-29 dBic	—	-24.3 dB	-15.37 dBic	-28.2 dBi	-18.8 dBi	-15.65 dBic	-18.3 dBi	-19.2/-19.1dBic
	Implant Depth	4 mm	45 mm	4 mm	—	10 mm	—	50 mm	5 mm	2 mm	5 mm	50 mm
	System	No	No	No	No	No	No	Yes	Yes	No	Yes	Yes

UHF: ultra high frequency; TCE: total conversion efficiency; NA: not applicable; MTM: metamaterial; η : conversion efficiency; D: Diameter; H: Height; —: not given

II. SYNTHESIS OF FULL PACKAGE CUBIC RECTENNA:

A. System Architecture:

In order to establish multi-channel biotelemetry between an external transceiver system and an implantable CRMS, simultaneous wireless functions of power and data telemetry should be robust. Fig. 2 presents the detailed architecture of the proposed CRMS, including power management and data management modules. RT Duroid 5880 substrate boards ($\epsilon_r=2.2$, $\tan \delta=0.0009$, $h=0.508\text{mm}$) forms the cube's six faces, and the top and bottom faces contain the circuit modules. The top face consists of power management circuitry installed with a DC combining circuit, rechargeable batteries for power harvesting, and a control unit to sync the power and data modules clock. The bottom face of the CRMS consists of data management circuitry and two different biosensors S_T and S_P to measure temperature [32] and pressure [33] vitals of the human body, transceiver IC, microprocessor, and memory IC.

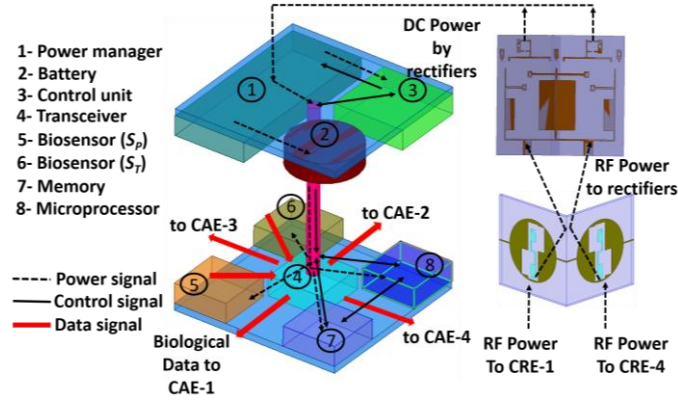


Fig. 2 Architecture of the proposed FPCR for simultaneous multi-channel biotelemetry functions.

To develop a biocompatible full package cubic rectenna (FPCR), in CRMS, rectifier circuits are designed on the backside of the substrate of the cubic antenna elements (CAEs), and the rectifier integrated CAEs are denoted as cubic rectenna elements (CREs). Further, the CRMS is enclosed in a biocompatible 0.2 mm thick zirconia ($\epsilon_r=27$) ceramic container. The coplanar topology of the CAEs provides room to design rectifiers on the other side of the substrate. To observe the coupling of CREs with the modules, batteries are modelled as metallic (PEC), while other microelectronic components (ICs) and central hollow cylindrical tubes (to pass connecting wires) are modelled as dielectric PVC. Each PCB is characterized by the same substrate material and has an overall thickness of 2 mm, including circuitry.

B. Implantable Cubic Rectenna Element Design:

The proposed CAE of the CRMS is designed on the substrate of size ($15 \times 15 \text{ mm}^2$) and comprises the circular ground plane of the radius (R) 5.2mm, which is coplanar with the metal strip in the middle acting as a patch, as shown in Fig. 3. The ground plane is loaded with a vertical rectangular slot ($9.5 \times 2.3 \text{ mm}^2$) to place a patch strip ($8.2 \times 1.1 \text{ mm}^2$) into the center of the ground plane. Two more asymmetrical rectangular slots

($4.25 \times 1.4 \text{ mm}^2$) are loaded to break the symmetry of the ground plane and obtain the circular polarization. A gap of 0.3 mm between the patch strip and the circular ground is utilized to power the antenna through the coplanar feed. All the CAEs of the CRMS are designed altogether in the shape of a cube, but for brevity, Fig. 3 shows the design evolution of only a single CAE. Note that the antenna design evolved in the presence of data and power management circuit modules. The substrate's front side is covered by the ceramic biocompatible zirconia layer of 0.2 mm thickness. The basic antenna topology is referenced from [34], which proposed the design of a cubic antenna; however, the system level study was missing for WPT and was not biocompatible for implantation.

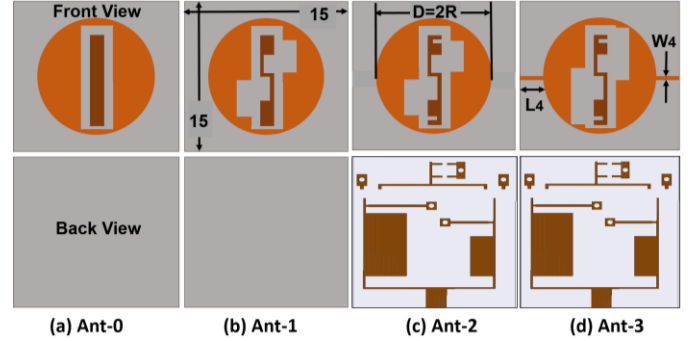


Fig. 3 Design evolution stages of CRE (Ant-3) of the proposed FPCR.

The design cycle is initiated with Ant-0 (Fig. 3(a)), where a patch strip is acting as a monopole, which can be approximated with a linear wire antenna so that the resonant frequency of this patch strip could become a function of its overall size, length, and geometry [35]. The simulated reflection coefficient ($|S_{11}|$) and axial-ratio (AR) of the design evolution stages are shown in Fig. 4. Ant-0 provides resonance with impedance matching below par at two frequencies, 3.7 and 6.9 GHz, and the radiations are linearly polarized. The resonating length of the patch strip and half of the rectangular slot in the ground merged together to excite the lower frequency, whereas only half of the rectangular slot excites the higher frequency. The current path length at both the resonances corresponds to $\lambda_g/4$, λ_g is wavelength in the medium. To shift the resonance to the lower side in the target ISM bands, Ant-1 (Fig. 3(b)) is designed. Ant-1 shifts the two frequencies to 2.7 and 6.2 GHz. Note that frequency miniaturization is achieved by introducing meandered sections in the patch strip and two additional rectangular slots in the ground, which elongated the respective current paths at both the resonances. Rectangular slots also generate CP radiation with AR 0.7 dB and 1.8 dB at frequencies 2.6 and 6.4 GHz, respectively.

To evolve the CAE into the CRE, a rectifier is designed at the backside of the substrate of Ant-1, which detunes the frequency response of Ant-1. Hence, Ant-2 (Fig. 3(c)) is designed to improve the results by contemplating the undesirable coupling with the rectifier circuit. The meandered patch strip is optimized by including two horizontal rectangular slits ($0.85 \times 0.3 \text{ mm}^2$) on the upper and bottom sides of the patch strip. The slits tune the resonating frequencies to 2.3 and 5.3 GHz by contributing a capacitive effect to the feed impedance and thus, boost the impedance matching in the presence of

circuit modules but detune the AR drastically in both the frequency bands. After that, Ant-3 (Fig. 3(d)) is designed where asymmetry in the rectangular slots is made more pronounced by further optimizing the dimensions. The slots split the fundamental mode in the two frequency bands into two near-degenerate orthogonal modes, and the asymmetric position of the two slots with respect to each other induces phase quadrature between the two orthogonal modes. This improved the AR to 0.8 dB and 0.2 dB at 2.45 GHz and 6.1 GHz, respectively, as evidenced by different slot configurations in Fig. 5. Ant-3 provides polarization diversified dual ISM band operation (RHCP waves at 2.45 GHz and LHCP waves at 5.8 GHz).

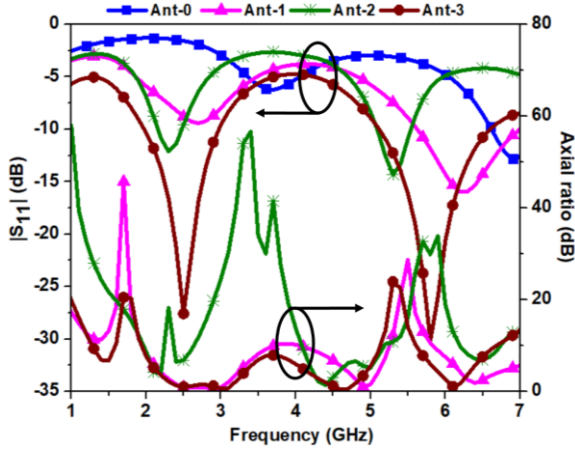


Fig. 4 Simulated $|S_{11}|$ and AR plot for Ant-0 to Ant-3(proposed).

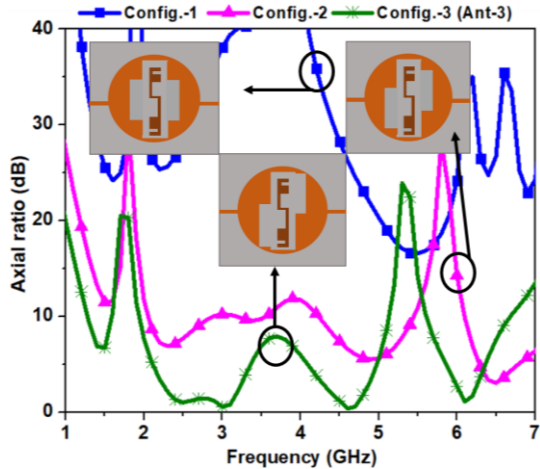


Fig. 5 Simulated A.R plot for asymmetrical slot configuration in CRE of the proposed FPCR.

Moreover, to facilitate the common ground potential among the four CREs, a 0.2 mm thick copper strip ($L_4 \times W_4$) is added to both sides of the CRE (see Fig. 3(d)). In this design, the radius of the CRE is not interfering significantly with the resonant frequency. The resonating frequency shifted in the target ISM bands with reasonable impedance matching as the inductive effect provided by the copper strip neutralizes the capacitive effect due to slits in the patch strip and renders the feed impedance completely resistive. Note that at both the resonant frequencies, the current travels in $\lambda_g/4$ monopole mode

(current direction remains the same on the corresponding path length between the adjacent maxima and minima) as evidenced from the surface current distribution on the proposed Ant-3, shown in Fig. 6. The -10 dB impedance bandwidth is from 1.94 – 3GHz and 5.1 – 6.6GHz which easily covers the 3-dB AR bandwidth from 2.23 – 3.23GHz and 5.8 – 6.3GHz at the central resonant frequency of 2.45 and 5.8 GHz, respectively. Finally, Ant-3 is the CRE of the proposed FPCR.

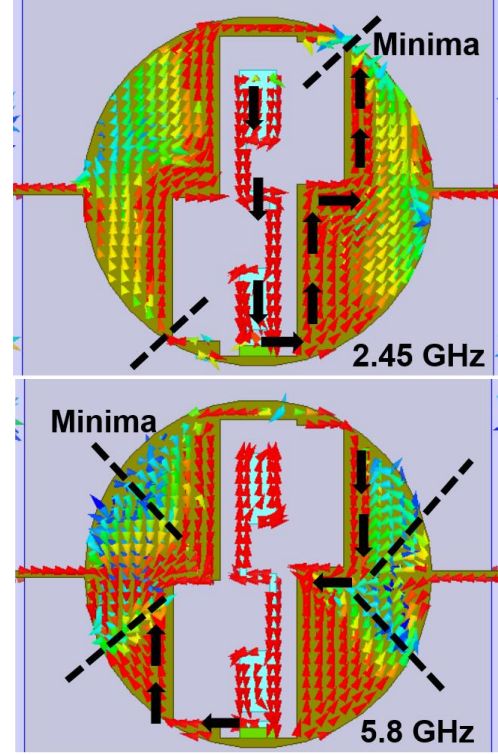


Fig. 6 Surface current distribution on CRE of the proposed FPCR (Red: high intensity; blue: low intensity current).

C. Dual Branch Rectifier Circuit Design

The layout and fabricated prototype of the proposed novel dual-branch rectifier circuit is shown in Fig. 7(a-b) and (c), respectively. The implantable circuit is designed on RT duroid 5880 substrate, having footprints $15 \times 15 \text{ mm}^2$, using Advanced Design System (ADS) software through electromagnetic (EM)/Circuit co-simulation. The rectifier circuit has been designed with a source impedance of 50Ω to avoid impedance mismatch and simplify its integration with the CAEs.

A matching network is very crucial for maximum power transfer to the load. Therefore, a separate impedance matching circuit has been designed for both resonant frequencies. Thus, the proposed rectifier could obtain acceptable conversion efficiency in both frequency bands for biomedical applications where the input power (P_{in}) could be in the order of -30 dBm . Generally, the Schottky diode has been used in rectifying circuits due to its low forward bias built-in voltage (V_{bi}) that supports low power operation [8] and fast switching response along with high cutoff frequency. V_{bi} is the diode junction voltage in the ON state. We have adopted a commercially available Schottky diode from BROADCOM with part no.

HSMS-2820-TRIG to design rectifier in this work. As per technical data-sheet, the diode has $V_{bi} = 0.34V$ and breakdown voltage, $V_b = 7V$, zero bias junction capacitance, $C_{jo} = 0.7pF$ with series resistance, $R_s = 6\Omega$. The low value of junction capacitance would minimize the effect of frequency on conversion efficiency [36]. The input impedance (Z_D) of the diode is $(57.8-j5.6)\Omega$ and $(30.4+j7.9)\Omega$ at 2.45 GHz and 5.8 GHz, respectively. Microstrip stubs are used to conjugate and match the antenna impedance with the rectifier impedance [16].

The two branches are designed to rectify the RF signal and achieve DC output simultaneously at the frequency of 5.8 GHz (branch with diode D_2) and 2.45 GHz (branch with diode D_1). Series inductors $L_{D1} \times W_{D1}$ (8.35×4.25) and $L_{D3} \times W_{D3}$ (5.25×2.5) and shunted inductors $L_{D2} \times W_{D2}$ (5.7×0.3) and $L_{D4} \times W_{D4}$ (3.75×0.3) at the diode's input in both the branches constitute the matching networks and DC block filter (input filter) from the diodes (D_1 and D_2), respectively. Note the microstrip dimensions are optimized to achieve the desired output [15]. Further, these two branches connect with the common shunt mounted capacitor $C_1 = 8.2 pF$ (output filter), which acts as a DC pass filter to pass only the DC power to load resistor (R_L) and reflect any RF leakage to the diode. The output DC voltage (V_{DC}) is taken across the optimized $R_L = 1 K\Omega$ placed in parallel with the capacitor.

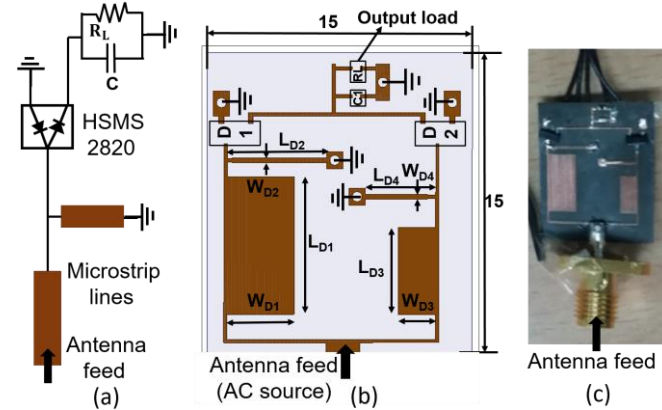


Fig 7. (a) Equivalent circuit of single branch rectifier (b) Proposed dual branch rectifier circuit layout (c) Fabricated prototype of the rectifier circuit.

D. Origin of the Cubic Geometry:

The proposed CRE in Fig. 3(d) could provide CP diversity in the broadside if placed at $\lambda_g/8$ apart from its mirror image (see Fig. 8(a)) on the substrate in the MIMO configuration. The proposed CRE radiates RHCP waves at 2.45 GHz and LHCP waves at 5.8 GHz, whereas the mirror image radiates orthogonally polarized waves (LHCP waves at 2.45 GHz and RHCP waves at 5.8 GHz). By interchanging the slots' positions, either LHCP or RHCP waves could be generated. However, the planar topology of the 2-element MIMO rectenna could provide CP diversity in both the frequency bands and in the broadside only. Moreover, incapable of providing spatial diversity to account for 360° coverage. Note that, typically, the implants are planar in one direction, but the planar (non-cubic) implementation will not hold the proposed principle of operation in 3D space effectively, as the planar geometries are more suitable for broadside coverage only.

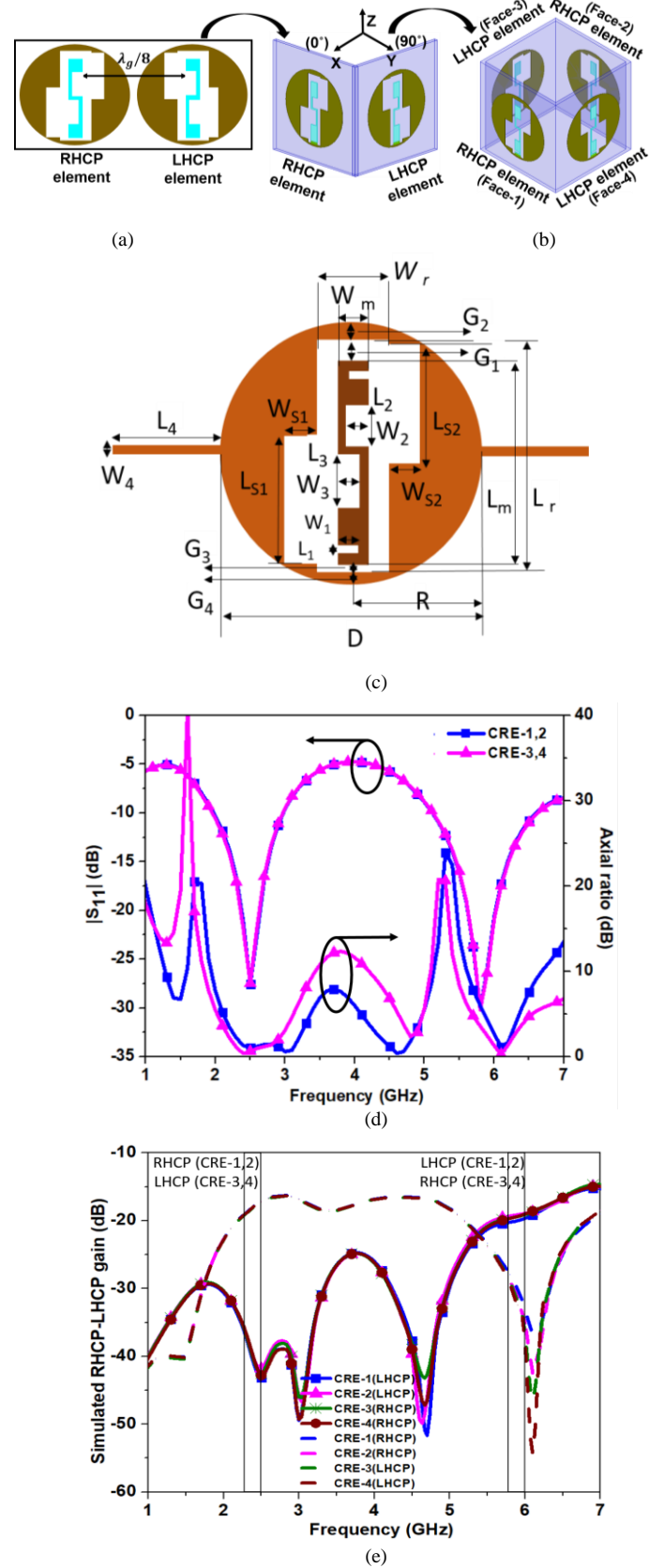


Fig. 8 Origin of the cubic geometry (a) 2-element planar MIMO (b) Proposed 4-element CRMS (c) Geometrical design of CRE of the proposed FPCR (d) Simulated $|S_{11}|$ and A.R plot of CRE-1,2 and -3,4 (e) Simulated RHCP-LHCP gain of CRE-1,2 and -3,4.

Therefore, the non-planar topology of the 4-element CRMS (see Fig. 8(b)) could provide both RHCP and LHCP polarization at both 2.45 and 5.8 GHz in a spatial quadrature (360°). Further, the cubic configuration could also improve the isolation between the CREs by compensating for the coupling issue due to the minimum gap of $\lambda_g/8$, compared to planar counterparts. Notably, the four communicating channels: 2.45 GHz (RHCP), 2.45 GHz (LHCP), 5.8 GHz (RHCP), and 5.8 GHz (LHCP), can be used simultaneously for data telemetry, wireless power transfer, and control signaling in biotelemetric applications.

Fig. 8(c) presents the geometrical design of the proposed CRE of the FPCR, which is placed on faces-1,2 (set-A) and the mirror image of CRE on faces-3,4 (set-B) or FPCR (see Fig. 8(b)). Physical dimensions are provided in Table II. CRE-i ($i = 1,2,3,4$) belongs to cubic face-i. Additionally, from Fig. 8(b), we can see the physical volume ($15 \times 15 \times 15 \text{ mm}^3$) of the FPCR (IMD) is only $\approx 17\%$ of the cubic-shaped IMDs designed successfully in [37], [38]. Hence, the physical size of the proposed FPCR is not a concern for muscle implantation. Fig. 8(d and e) shows the simulated $|S_{11}|$, AR, and RHCP-LHCP gain of the CRE of both set-A & B, respectively. From the results, it can be concluded that all the CREs would perform identically to each other with diverse CP radiation in orthogonal space. Note that the working mechanism of Fig. 8(a and b) is explained with free space in the vicinity of the MIMO antenna, whereas the results in Fig. 8(c-e) are presented with human arm phantom model in the vicinity. Further, in this article, all the simulated and measured results stand for CRE-1 only unless mentioned, for brevity, but support all other CREs that are designed altogether.

Table II
DESIGN PARAMETERS OF THE PROPOSED CRE (IN MM)

D	10.4	L_{S1}	4.5	L_2	1.5	G_3	0.3
R	5.2	W_{S1}	1.7	W_2	0.9	G_4	0.3
L_r	9.5	L_{S2}	4.5	L_3	2.1	L_4	2.3
W_r	2.3	W_{S2}	1.7	W_3	0.9	W_4	0.2
L_m	8.2	L_1	0.3	G_1	1	--	--
W_m	1.1	W_1	0.9	G_2	0.6	--	--

E. External Transmitter Antenna

In the far-field, the external antenna as T_x should be able to communicate effectively with the proposed FPCR implanted inside the human arm at a fixed location to conduct power and data telemetry operations on different channels in terms of diverse CP in NLOS directions. Therefore, in this work, any CP diversified dual ISM band (2.45 and 5.8 GHz) antenna designed in free space would be the best fit to play the role of T_x . Hence, the design of T_x ($50 \times 50 \times 1.0 \text{ mm}^3$) is chosen from [39]. The T_x is designed in the simulator, and the same simulated and measured results are reproduced as demonstrated in [39]. The fabricated prototype and the measurement scenario are shown in Fig. 9. The antenna transmitting at 2.45 GHz with RHCP polarization and LHCP polarization at 5.8 GHz is designated as T_{x_1} , whereas the antenna behaving conversely is T_{x_2} . Hence, T_{x_1} and T_{x_2} are characterized as standard transmit antennas, and their communication with CRE-i of the proposed FPCR is demonstrated in subsection-C of section-IV, where received

power levels in dBm at CRE-i are established. Remarkably, in far-field WPT, where propagating modes are developed in both free-space and tissue layers, T_x is not required to be designed in close proximity to high permittivity tissues like in mid-field range WPT [40], which works by developing propagating modes inside tissues only.

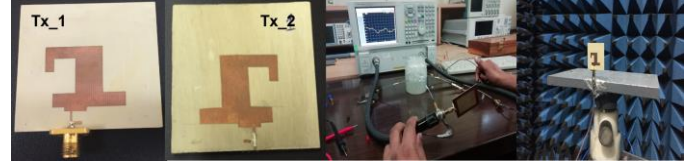


Fig. 9 Fabricated prototype of T_{x_1} and T_{x_2} and measurement setup. The T_x design is chosen from [39].

III. SIMULATION AND RESULTS

The proposed FPCR is placed at the centre of a homogeneous canonical (skin-fat-muscle) tissue phantom model of the human upper arm. The frequency domain simulations are carried out in the EM simulator Ansys HFSS (v 19.3) using a workstation (32 cores and 1-TB RAM). The lumped ports excite the CREs for simplicity, and the phantom model in the shape of a cylinder ($R = 50\text{mm}$, $H = 300\text{mm}$, $R_{\text{skin}} = 50\text{mm}$, $R_{\text{fat}} = 45\text{mm}$, $R_{\text{muscle}} = 40\text{mm}$) considered the effect of free space in the vicinity by including radiation box ($310 \times 110 \times 110 \text{ mm}^3$) as shown in Fig. 10. To check feasibility at different implantation sites in a human body, the tissue model also adopted the shape of a cube of size ($100 \times 100 \times 100 \text{ mm}^3$) for chest implantation.

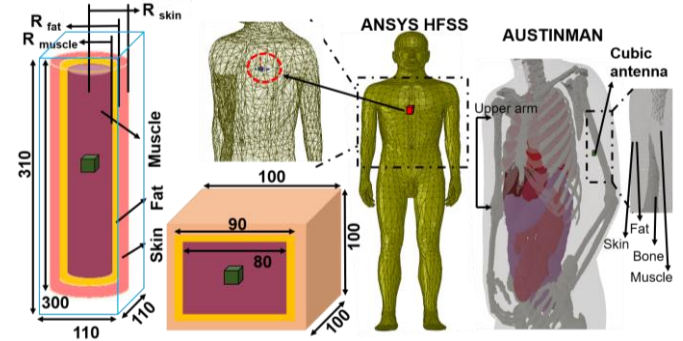


Fig. 10 Canonical and realistic (anatomical) human body models utilized as simulation enclosure.

Note the bone tissue layer is not inserted inside muscles in the cylindrical model as the bone layer did not significantly affect the cubic antenna's results in our previous work [34]. The electrical properties of the tissues are frequency-dependent and assigned corresponding to the frequency of 2.45 GHz from [41] to compensate for impedance mismatch at higher frequencies as the dielectric constant of tissues varies inversely compared to frequency. Further, for impedance matching of CREs with the tissue models, the cube is filled with solid artificial tissue emulating material bearing electrical properties with $\epsilon_r = 30-40$, and conductivity (σ) 1-10 S/m across the band 500 MHz–10 GHz [40]. The final optimized geometry of the proposed FPCR in the canonical arm model is also simulated and validated in a

realistic heterogeneous environment of an anatomical model of the human body, AustinMan v2.6 (arm implantation) [42] and HFSS model (chest implantation) [43]. Note the antenna is placed at an implantable depth of 30 mm during the simulation in both the digital realistic models. Here, numerical analyses for voxel-based AustinMan and surface-based HFSS models are conducted using Computer Simulation Technology (CST) Studio Suite and Ansys High Frequency Structure Simulator (HFSS), respectively.

Fig. 11 compares simulated $|S_{11}|$ and A.R for CRE-1 of the proposed FPCR in simplified homogeneous and realistic heterogeneous phantom models. Resonant frequency for $|S_{11}|$ in the cylinder and cubic model is similar at both frequencies and does not encounter any shift. But, in both the realistic models, $|S_{11}|$ shifts to a lower frequency due to the high ϵ_r value of surrounding tissues, without significant change in impedance value. On the other side, the AR value in the homogeneous models is almost the same at 5.8 GHz, but the value degrades to 5 dB at 2.45 GHz in the cubic model. Also, similar degradation in A.R is observed in both the realistic models but with a slight shift to the lower frequency. Nevertheless, the AR detuning can be administered by further optimizing the dimensions of the rectangular slots and rearranging the asymmetric position of the two slots with regard to each other. Hence, these observations validate the capability of FPCR to function at different implantation sites in the real human body.

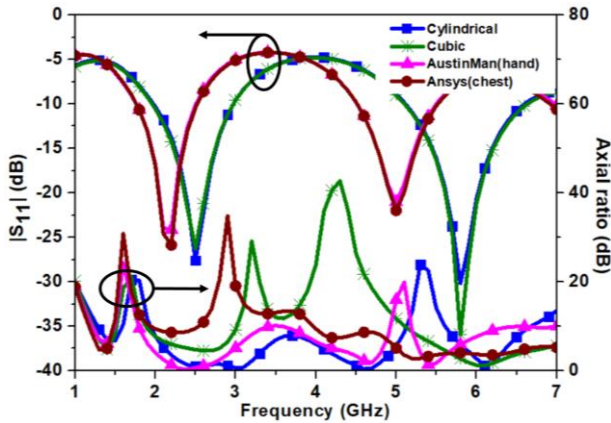


Fig. 11 Simulated $|S_{11}|$ and A.R plot of CRE of the proposed FPCR in different simulation enclosures. (Cylindrical shape: mimic hand; Cubic shape: mimic chest)

For practical considerations, batteries and circuitry inside FPCR are placed in such a way that they could not degrade antenna performance significantly as the sizes of CREs are comparable. As shown in Fig. 12(a), a pronounced effect on the circuit ICs is not observed at both 2.45 and 5.8 GHz ISM frequencies, where the maximum electric field of 15 V/m can be seen mostly over the surface of CREs only. As the circuit ICs are placed orthogonal to the antenna elements and due to wide impedance bandwidths of CREs with good impedance match at both the frequencies, the field coupling that could lead to antenna detuning is negligible.

The feasibility of the diversity performance of CREs in the proposed MIMO FPCR can be achieved if the radiation patterns of all the CREs do not overlap each other. The 3-D radiation pattern of the proposed FPCR in the canonical arm model is

shown in Fig. 12(b), which justifies a low correlation coefficient among CREs in FPCR due to diverse radiation patterns in orthogonal directions. Thus, FPCR could receive power effectively from the off-body LOS/NLOS directions.

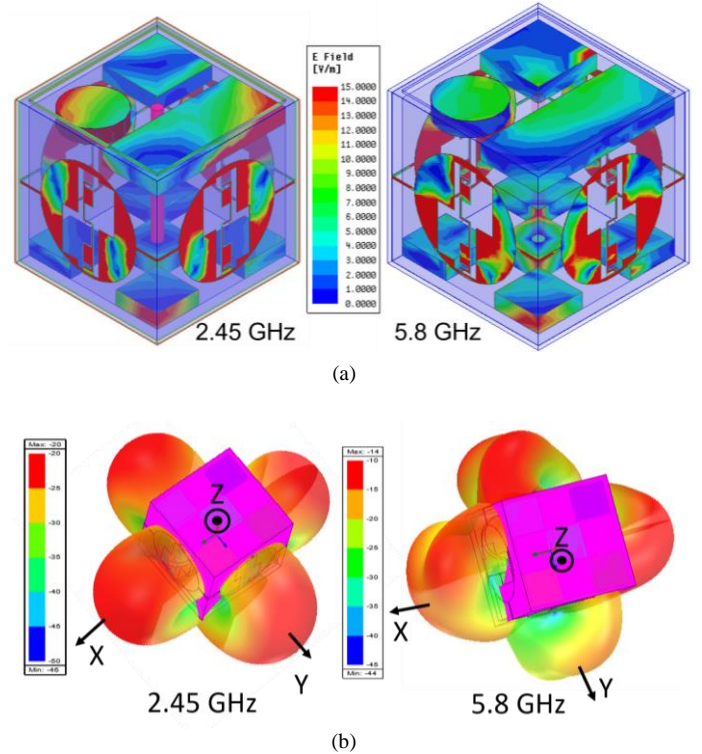


Fig. 12 (a) Electric field distribution on the circuit ICs and CREs (scale: V/m), (b) 3D radiation patterns of individual CREs of the proposed FPCR (scale: dB).

IV. MEASUREMENT AND RESULTS

A. Rectifier Measurement

For experimental validation in free space, the proposed rectifier circuit is fabricated on one side of a substrate, and CAE is fabricated on the opposite side to consider the influence of the copper layer of the antenna on the distributed elements of the rectifier circuit. At this stage, the feeding ports of the CAE and rectifier are not interconnected, and the circuit elements are grounded by providing a connection to the ground of the rectifier feed port (SMA connector).

$$\eta(\%) = \frac{V_{DC}^2}{R_L \cdot P_{in}} \times 100 \quad (1)$$

A microwave signal generator Tektronix TSG 4106A (DC - 6 GHz) feeds the rectifier's input port, and output DC voltage is measured across R_L . As the input power, input impedance, diode losses, and output load drive the rectifier's conversion efficiency [15], [16]; the RF-to-DC conversion efficiency (η) is calculated using Eq. (1), where, V_{DC} is the output DC voltage and P_{in} is the input power to the rectifier. The measured output DC voltage values of the rectifier and corresponding calculated conversion efficiency as a function of input power are shown in Fig. 13, and a good agreement between the simulated and measured results is observed. High efficiency of ~70% and

0.2V as V_{DC} has been achieved at both frequencies for low input power of -15 dBm with an optimized $R_L = 1 \text{ K}\Omega$. Further, using the proposed rectifier, ~60% conversion efficiency could be achieved easily for a broad range of input power (-20 dBm to -10 dBm). But, for reference high input power of 0 dBm, efficiency drops to 40% and 42% with $V_{DC} = 0.5\text{V}$ and 0.6V at 2.45 and 5.8 GHz, respectively; and beyond 20 dBm power, the diode approaches $V_b/2$ (3.5V) and enters into saturation. Although the matching losses are ignored for simplicity, 100% RF power cannot be converted to the useful DC power. Moreover, the output DC power measured across R_L is restricted by $P_{DC} < V_b^2/4R_L$.

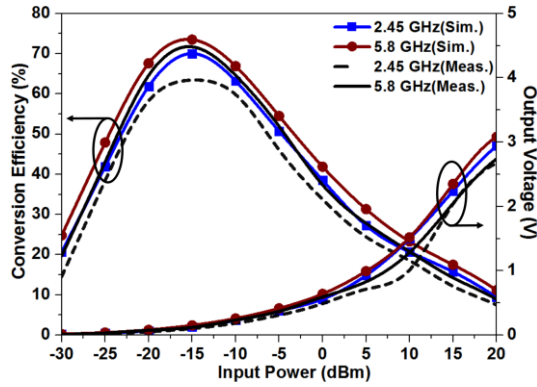
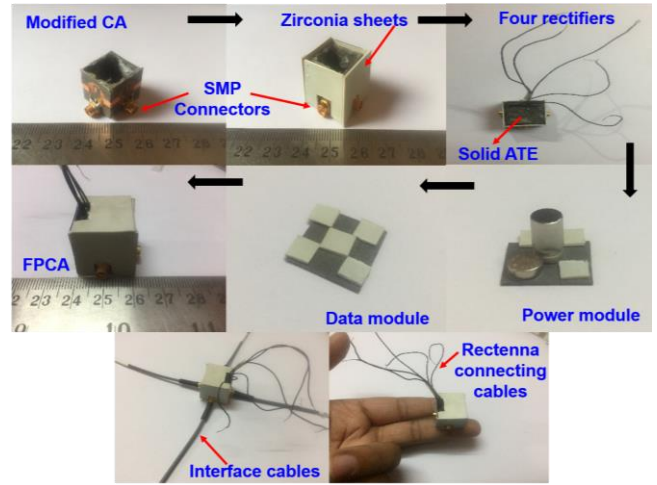


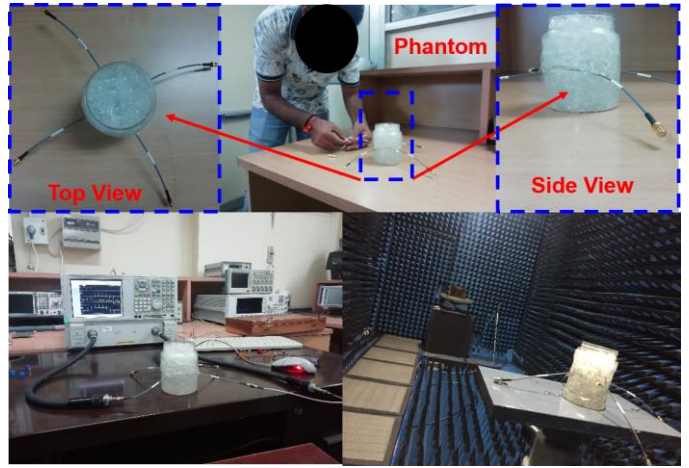
Fig. 13 Comparison of simulated and measured conversion efficiency and output DC voltage of the rectifier.

B. FPCR Measurement

Four proposed CREs are fabricated on RT duroid substrate ($15 \times 15 \text{ mm}^2$) separately, and the cubic shape is obtained manually, as shown in Fig. 14(a). Note that feed ports of rectifier circuits are connected to the CAEs through a metallic pin [13], which could cause minimal transition loss at each interconnection at both frequencies, but it is ignored for simplicity. To have consistency with the simulation scenario, 3D printed dummy circuit components are utilized as circuit modules, and the cube is filled with custom made solid dry material, which is prepared by following the steps mentioned in Fig. 10 of [40]. Subsequently, the biocompatible FPCR is obtained by manually fixing 3D-printed zirconia plates in a cubic configuration using adhesive glue, ensuring that the testing phantom fluid could not enter the zirconia cubic casing. The measurement is conducted by placing the FPCR inside a cylindrical container carrying a semi-solid canonical 3-layer phantom (gel) to mimic the cylindrical model of the human upper arm taken in the simulation, shown in Fig. 14(b). The measured electrical properties of the phantom layers are given in Table III, which are in close agreement with the properties referenced from [41], [44]. We have adopted the preparation procedure for phantom and solid dry material from [44], whereas the properties are measured through the open-ended coaxial probe technique demonstrated in [45]. At an instant, the Agilent N5230A power network analyzer excited a single CRE through a subminiature moxley surface mount plug with $50 \text{ }\Omega$ impedance while other CREs were connected to the matched terminals.



(a)



(b)

Fig. 14 (a) Fabricated prototype of the proposed FPCR at different intermediate stages (b) Near-field and far-field measurement setup.

Table III
MEASURED DIELECTRIC PROPERTIES OF PHANTOM LAYERS

Tissue layers	2.45 GHz		5.8 GHz	
	ϵ_r	σ (S/m)	ϵ_r	σ (S/m)
Skin	35.60	0.92	32.68	2.79
Fat	5.41	0.17	5.61	0.40
Muscle	50.98	1.26	47.17	4.98

Fig. 15(a) shows that the measured -10dB bandwidth of $|S_{11}|$ is from 2.2 to 3 GHz (32.65%) and 5.2 to 6.6 GHz (23.33%), smoothly follows the simulated bandwidth at the central frequency of 2.45 and 6 GHz in both the ISM bands. The measured 3dB bandwidth of A.R is from 2.1 to 3.1 GHz (40.82%) and 5.7 to 6.5 (13.33%). In the graph, the disparity of 2 to 4% in the measured impedance and AR bandwidths owes to the defects in the fabricated prototype of FPCR. It includes substrate loss and inconsistent measurement setup, which is irresistible to soldering tolerances, assembly error, devoid of accurate electrical properties due to imperfect phantom preparation, adapter cable losses, and inappropriate handling of

measuring devices. In Fig. 15(a), the measured far-field total gain is -19.2 dBi and -19.1 dBi in the broadside of CRE-1 at both the central frequencies, showing similar behavior and closely matching the simulated gain of -16.9 dBi and -19.3 dBi, respectively. The wide bandwidths and sufficient gain of the proposed FPCR in measurements have provided satisfactory results as evidence of the fruitfulness of the proposed work for biomedical applications.

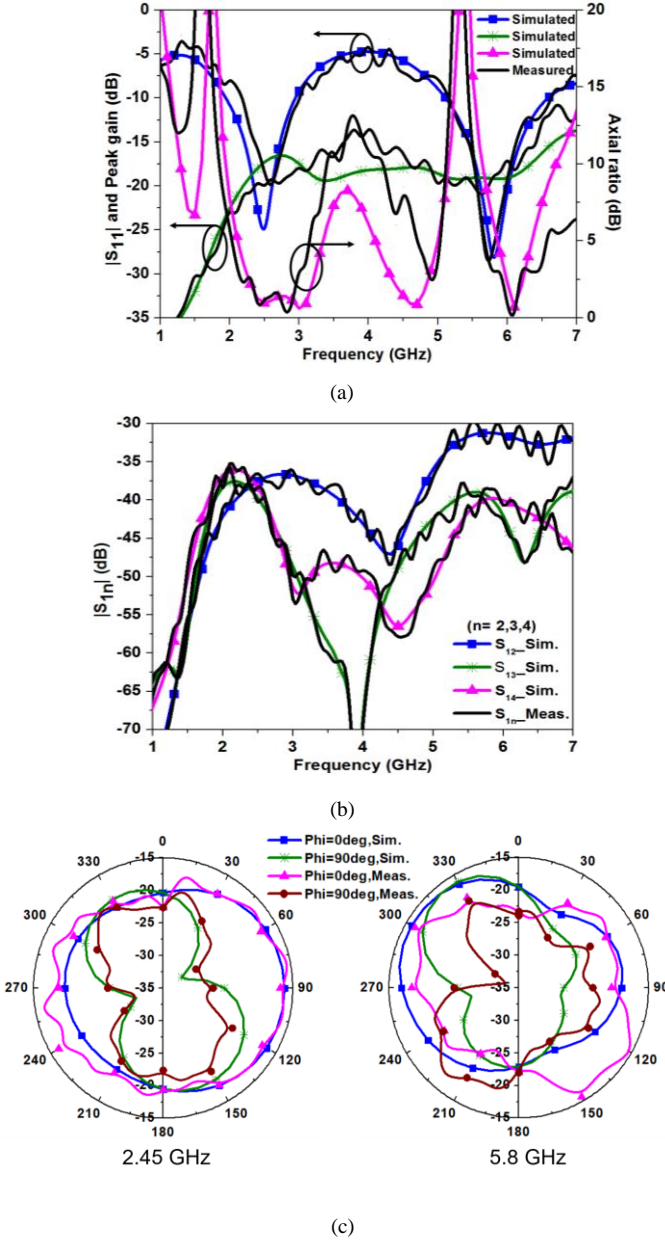


Fig. 15 Comparison of simulated and measured (a) $|S_{11}|$, total gain and A.R plot of CRE-1 (b) isolation plot between CREs (c) 2D radiation pattern plot of CRE-1 of the proposed FPCR in the 3-layer phantom gel.

To guarantee the MIMO performance, a minimum coupling of -15 dB is considered enough [46]. But, due to the strategic placement of CREs in a cubic configuration, the measured mutual coupling (S_{1n}) among the CREs is below -30 dB at both the frequencies of 2.45 and 6 GHz. The measured results follow closely with the simulated results, as shown in Fig. 15(b).

Hence, all the CREs in the proposed FPCR could work altogether as an efficient MIMO antenna system. Fig. 15(c) shows the simulated and measured far-field 2D radiation patterns measured inside an anechoic chamber. In broadside ($\theta=0^\circ$ for CRE-1), which is a desired off-body direction, the measured patterns for CRE-1 in phantom at 2.45 and 6 GHz in both E- ($\phi=0^\circ$) and H- ($\phi=90^\circ$) planes are somewhat distorted at both the frequencies, which may be due to the clitch in the rotation of the cylindrical container in which FPCR is embedded, where the gain value precedes to -23dB ($\theta=0^\circ$). It is observed that the overall radiation pattern due to the FPCR is isotropic at both frequencies if all the CREs work altogether, thus, making the proposed FPCR the most suitable IMD to handle all LOS/NLOS directions.

C. Rectenna Measurement

The T_x and R_x antennas with circular polarizations with respect to each other could communicate effectively [47]; therefore, in simulation, T_{x_2} is placed in LOS at a distance (d) of 500 mm from CRE-1 of FPCR. Subsequently, received power (P_{RF}^i) is recorded at different angles by CREs with respect to the fixed location of T_{x_2} to take into account the human arm's random mobility. To enable wireless power transfer, the transmission ($|S_{21}|$) and reflection coefficient ($|S_{11}|$) as given in Eq. (2) [16] can provide the maximum power transfer efficiency (PTE) of the well matched communication system. As the T_x utilized in this work is impedance matched, having $|S_{11}|$ of -18.3 dB and -30.6 dB at 2.45 and 5.8 GHz, respectively; therefore, $|S_{11}|$ can be ignored for simplicity.

$$PTE(\%) = \frac{|S_{21}|^2}{1 - |S_{11}|^2} \times 100 \quad (2)$$

As shown in Fig. 16, the simulated and measured P_{RF}^i levels due to CRE- i of the FPCR are given in Table IV. These values were noted when the measurement was conducted; however, the P_{RF}^i levels can differ if either the measurement scenario or transmit power (P_T) changes. Measured values are 2 to 3 dBm lower than simulated values, and the maximum P_T is 30 dBm in both simulation and measurement. Note that P_T can be increased to obtain higher received power. However, high transmit power could not meet the safety standards for biomedical applications. Further, the P_{RF}^i levels at 5.8 GHz are higher than 2.45 GHz due to high radiation efficiency at the higher frequency. Therefore, the PTE due to the single CRE of the proposed FPCR system lies in the range of 0.00003% to 0.014% depending on the LOS angle with respect to the external antenna. The dielectric mismatch between tissue layers and free space ($\epsilon_r=1$) reflects most of the radiated power back towards the T_x and thus, reduces the overall PTE. Note simulation and measurement are also conducted by keeping T_{x_1} in LOS with CRE-4, and this configuration also provided similar received power values at the CREs but is not shown here to avoid repetition.

Fig. 17 shows the measurement setup for WPT, where the proposed FPCR is implanted at 50 mm depth in the muscle layer of the 3-layer phantom, with CRE-1 in LOS with T_{x_2} . We measured the output DC voltage of the FPCR using a

multimeter, and Eq. (3) provided the TCE [15]. It is to be noted that TCE is measured with respect to the power transmitted (P_T) to the T_{x_2} . At P_T of 30 dBm, the CRE-1 produces V_{DC} of 0.51 V and 0.57 V at 2.45 GHz and 5.8 GHz, respectively, across 1 K Ω load for a transfer distance of 500 mm. Therefore, the maximum measured TCE due to CRE-1 in LOS with T_{x_2} is 0.026% and 0.033% with the converted DC power ($P_{DC} = V_{DC}^2 / R_L$) of 0.26 mW and 0.33 mW at 2.45 GHz and 5.8 GHz, respectively. Further, it is also observed that other CREs in NLOS directions (T_{x_2} makes $\angle 90^\circ$ with CRE-3,4 and $\angle 180^\circ$ with CRE-2) would provide lower TCE and P_{DC} values compared to CRE-1.

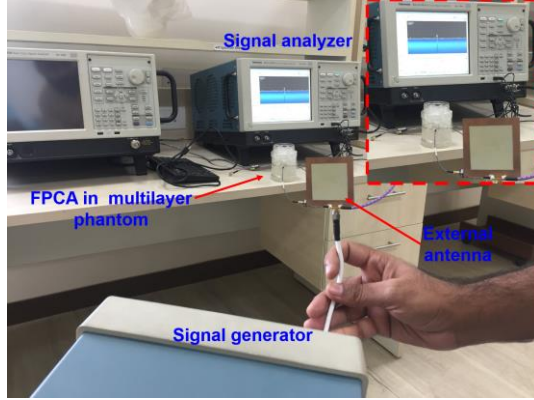


Fig. 16 Setup to measure received power (in inset) values by the CREs of the proposed FPCR (CRE-1 is in LOS with T_{x_2}).

Table IV
RECEIVED POWER LEVELS WHEN T_{x_2} IN LOS WITH CRE-1

$T_x \rightarrow R_x$	$T_{x_2} \rightarrow \text{CRE-1}$		$T_{x_2} \rightarrow \text{CRE-3}$		$T_{x_2} \rightarrow \text{CRE-4}$		$T_{x_2} \rightarrow \text{CRE-2}$	
LOS angle	0°		90° / 270°		90°		180°	
Freq.(GHz)	2.5	5.8	2.5	5.8	2.5	5.8	2.5	5.8
$P_{RF_sim.}$ (dBm)	-21.0	-8.6	-26.2	-17.4	-26.9	-18.6	-34.3	-14.0
$P_{RF_meas.}$ (dBm)	-23.7	-11.1	-29.4	-19.6	-28.6	-19.9	-35.8	-16.7

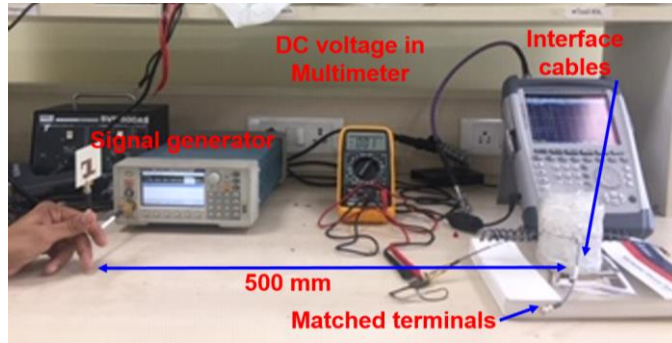


Fig. 17 Measurement setup for WPT (CRE-1 is in LOS with T_{x_2}).

$$TCE(\%) = \frac{V_{DC}^2}{R_L \cdot P_T} \times 100 \quad (3)$$

D. Power Enhancement using DC Combiner

The proposed FPCR is required to have high RF-DC conversion efficiency with high DC voltage (3-5 V) to meet the standard power requirements of all the ICs in power and data

modules in a multitasking biotelemetry. As the overall P_{RF} due to the FPCR will increase if all the CREs receive power altogether, improvement in TCE due to the two topologies of rectenna interconnections is investigated. Four CREs are connected in series and parallel configurations, as demonstrated in Fig. 18(a) and (b). For maximum conversion efficiency, R_L is chosen as 4 K Ω and 0.25 K Ω in series and parallel topology, respectively.

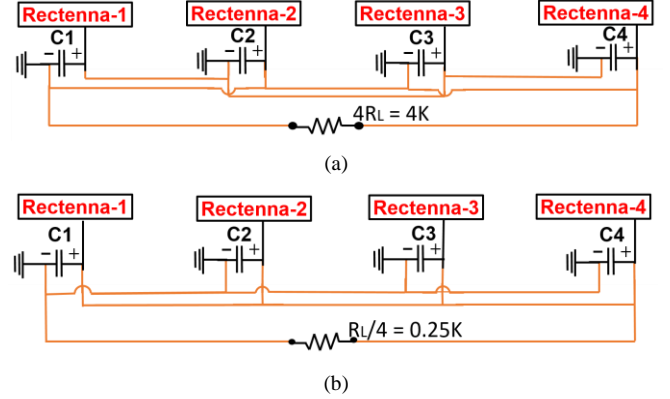


Fig. 18 Schematic of the four CREs of the proposed FPCR connected in (a) series and (b) parallel configuration.

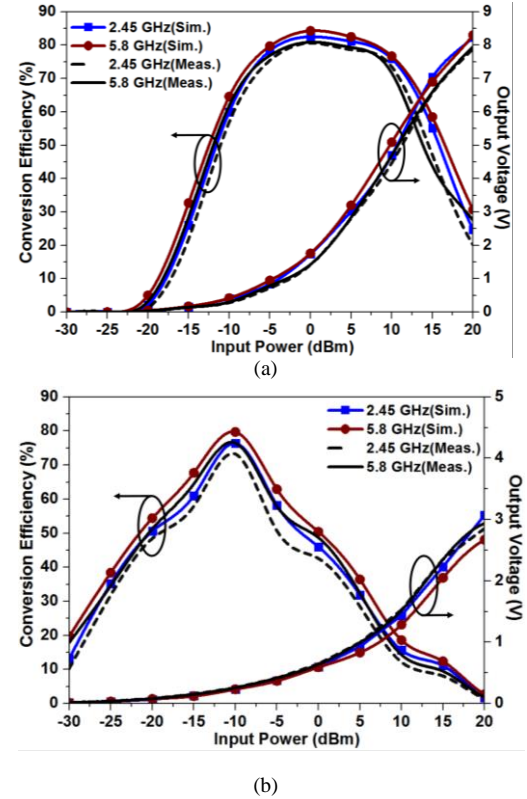


Fig. 19 Comparison of simulated and measured conversion efficiency ' η ' and output DC voltage for the proposed FPCR when CREs are connected in (a) Series and (b) Parallel topology.

Fig. 19(a) shows that for series connection, simulated V_{DC} due to the FPCR is 1.74/1.76V, whereas the measured V_{DC} is 1.42/1.43V at 2.45/5.8 GHz, respectively. Note that the input power to all the rectifiers is the same ($P_{in} = 0$ dBm) in the simulation but differs in the measurement. The conversion efficiency (η) improves to $\sim 80\%$ at 0 dBm input power at both

frequencies. As the input power (P_{in}) could be higher if P_T is increased, therefore, at 10 dBm input power, the simulated and measured V_{DC} reaches to ~ 5 V.

For parallel connection, Fig. 19(b) shows that both simulated and measured DC voltage values are the same, that is, 0.59/0.64V at 2.45/5.8 GHz, respectively. These values are also consistent with the values of the single rectifier. The conversion efficiency also improves to $\sim 80\%$ but at a low input power of -10 dBm. Hence, the results follow the theoretical expectations where the series topology should provide n times the output voltage of a single rectifier for n interconnected rectifiers, but parallel topology should provide the same DC voltage as of a single rectifier if all the rectifiers are the same and receive the same P_{in} [21]. Therefore, it can be concluded from the results in Fig. 19 that the overall V_{DC} , TCE, and P_{DC} (shown in Table V) due to the proposed FPCR can be enhanced for higher P_{in} if all the CREs are interconnected in a series configuration. But, in a parallel configuration, a similar enhancement is observed at lower P_{in} values. In summary, when CRE-1 is in LOS with T_{x_2} ($P_T=30$ dBm), in series connection, the measured V_{DC} , TCE, and P_{DC} due to the FPCR are enhanced by 0.91/0.86V, 0.024/0.017%, and 0.24/0.18mW at 2.45/5.8 GHz, respectively, as compared to single CRE-1. On the other side, in parallel connection, the same parameters of the FPCR are enhanced by 0.08/0.07 V, 0.114/0.127 %, and 1.13/1.31 mW, respectively.

Table V
WPT RESULTS OF THE PROPOSED FPCR USING DC COMBINER

	V _{DC} (V)		TCE (%)		P _{DC} (mW)	
Series Topology (R _L = 4 K)						
Freq. (GHz)	2.45	5.8	2.45	5.8	2.45	5.8
Simulated	1.74	1.76	0.075	0.077	0.75	0.77
Measured	1.42	1.43	0.05	0.05	0.50	0.51
Parallel Topology (R _L = 0.25 K)						
Simulated	0.59	0.64	0.14	0.16	1.39	1.64
Measured	0.59	0.64	0.14	0.16	1.39	1.64
Single CRE-1						
Measured	0.51	0.57	0.026	0.033	0.26	0.33

- **Series topology:** voltage, efficiency, and power due to the FPCR where CRE-1 is in LOS with T_{x_2} and the four CREs are connected in series.
- **Parallel topology:** voltage, efficiency, and power due to the FPCR where CRE-1 is in LOS with T_{x_2} and the four CREs are connected in parallel.
- **Single CRE-1:** voltage, efficiency, and power due to CRE-1 only, which is in LOS with T_{x_2} .

V. SAFETY CONSIDERATIONS

To meet the safety guidelines, with respect to the proposed implantable FPCR, we have estimated the FCC and IEEE approved power levels in terms of effective isotropic radiated power (EIRP), time-averaged surface exposure of tissue, and power absorption in tissue (SAR). FCC restricts the time-averaged (~ 30 min) maximum permissible exposure (MPE) of tissue surface to any specified radiating transmitter. At a frequency of 2.45 and 5.8 GHz, the flux density of the MPE should be 10 W/m^2 [48]. The maximum EIRP limit (36 dBm) for T_x with P_T of 30 dBm as restricted by FCC part 15 [48], [10], limits the minimum distance (d) of the IMD from T_x to be 178 mm for power telemetry in case of WPT according to Eq. (4).

$$MPE = \frac{EIRP}{4\pi d^2} \leq 10 \frac{W}{m^2} \quad (4)$$

To avoid the violation of the MPE threshold, in our case, the T_x should transmit power from at least 143 mm distance from any CRE of the proposed FPCR, as the EIRP of EA is ~ 34 dBm at both 2.45 and 5.8 GHz frequency. Note, to increase the minimum distance for the fixed MPE (10 W/m^2), only gain improvement could achieve the EIRP limit of 36 dBm for T_x as the increase in P_T would increase the tissue surface exposure and power absorption in tissue.

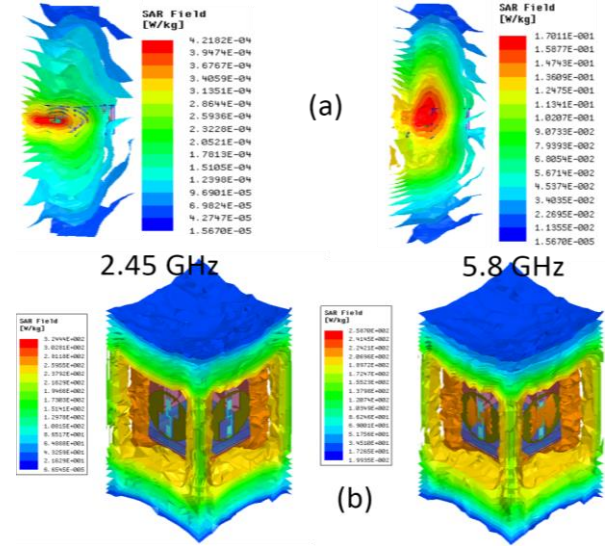


Fig. 20 ASAR analysis in canonical arm model (a) 1g ASAR when T_x is excited (b) 10g ASAR when FPCR is excited (scale: W/kg).

As the implanted FPCR will be utilized as both T_x (for data telemetry) and R_x (for power telemetry) hence, SAR distribution is also evaluated in the canonical arm model by exciting both T_x (located at $d = 500$ mm) and FPCR, alternatively. To consider patient safety, IEEE has given two standards restricting the maximum power absorption by human tissues. IEEE C95.1-1999 controls average SAR (ASAR) $< 1.6 \text{ W/Kg}$ over any 1g of cube shaped tissue, whereas IEEE C95.1-2005 limits ASAR $< 2 \text{ W/Kg}$ over any 10g of tissue [10]. In this study, for brevity, 1g ASAR distribution is evaluated due to the T_x and 10g ASAR due to the FPCR, as shown in Fig. 20(a) and (b), respectively. Note the dosimetric quantity simulations are performed in HFSS as no experimental procedure has been established to measure SAR at present [3]. The peak 1g ASAR values are 0.0004 W/Kg and 0.17 W/Kg at 2.45 and 5.8 GHz, respectively, when 1W power is given to the T_x . Further, the peak 10g ASAR value due to a single CRE is 258.70 W/Kg and 324.44 W/Kg , respectively, when 1W power is given to the single CRE.

Considering the IEEE C95.1-2005 restrictions, to perform data telemetry, the maximum power that could be given to the single CRE is 7.73 mW (8.8 dBm) and 6.16 mW (7.8 dBm), respectively. Therefore, the maximum power that could be given to the whole FPCR is 30.92 mW (14.9 dBm) and 24.64 mW (13.9 dBm), respectively. Moreover, considering the IEEE C95.1-1999 restrictions, to perform power telemetry from a

distance of 500mm, the maximum P_T that could be given to the T_x is 1330mW (31.2 dBm) and 1060mW (30.2 dBm), respectively. Note, as the maximum P_T of 30 dBm is allowed for T_x , and a maximum power of -16 dBm is allowed for each CRE for implantable applications in practical [49]; therefore, SAR due to both T_x and FPCR is not problematic.

VI. CONCLUSION

In this paper, an integrated rectenna MIMO system in non-planar cubic topology operating in dual ISM frequency bands of 2.45 and 5.8 GHz is explored and designed. The strategic design of the proposed cubic rectenna system is capable of receiving both RHCP and LHCP signals from the orthogonal space (360°) and demonstrates far-field WPT. Further, the four rectenna elements are interconnected in series and parallel configurations to improve the conversion of RF-DC power. The WPT system comprises an implantable FPCR as a R_x and an external antenna as a T_x . The T_x is chosen from the literature and characterized as a standard transmit antenna after reproducing the results from its fabricated prototype.

The Schottky diode based dual branch rectifier is designed in ADS to rectify low RF power at both frequencies in the order of -20 to -10 dBm with an optimized R_L of $1\text{ K}\Omega$. The fabricated rectifier achieved $\eta = \sim 70\%$ at -15 dBm input power at both frequencies. The FPCR prototype is measured in skin-fat-muscle phantom in the presence of 3D printed circuit components. When FPCR is positioned at a distance of 500mm from the T_x (with CRE-1 in LOS with T_x), wireless power is delivered to the FPCR from the T_x ($P_T = 30$ dBm). The proposed FPCR provided the measured P_{RF} due to CRE-i and achieved PTE in the range of 0.00003% to 0.014% in both the frequency bands. Further, the single element (CRE-1) achieved the measured TCE of 0.026% and 0.033% , with P_{DC} of 0.26 mW and 0.33 mW at 2.45 GHz and 5.8 GHz , respectively. Furthermore, P_{DC} is improved by $0.24/1.13\text{ mW}$ and $0.18/1.31\text{ mW}$ when all the CREs are interconnected in a series/parallel configuration, respectively. Additionally, human safety is ensured by analyzing SAR distribution in an arm tissue model.

ACKNOWLEDGEMENT

The authors would like to thank the Council of Scientific and Industrial Research (CSIR), India for the financial assistance for this work (SRF grant: 09 / 263 (1181) / 2019-EMR-I). This work was also partially supported by a grant of the Romanian Ministry of Education and Research, CNCS - UEFISCDI, project number PN-III-P4-ID-PCE-2020-0404, within PNCIDI III".

REFERENCES

- [1] D. Panescu, "Emerging technologies: Wireless communication systems for implantable medical devices," *IEEE Eng. Med. Biol. Mag.*, vol. 27, no. 2, pp. 96–101, 2008, doi: 10.1109/EMB.2008.915488.
- [2] B. J. DeLong, A. Kiourti, and J. L. Volakis, "A Radiating Near-Field Patch Rectenna for Wireless Power Transfer to Medical Implants at 2.4 GHz," *IEEE J. Electromagn. RF Microwaves Med. Biol.*, vol. 2, no. 1, pp. 64–69, 2018, doi: 10.1109/JERM.2018.2815905.
- [3] G. Sun, B. Muneer, Y. Li, and Q. Zhu, "Ultracompact Implantable Design with Integrated Wireless Power Transfer and RF Transmission Capabilities," *IEEE Trans. Biomed. Circuits Syst.*, 2018, doi: 10.1109/TBCAS.2017.2787649.
- [4] K. Agarwal, R. Jegadeesan, Y. X. Guo, and N. V. Thakor, "Wireless Power Transfer Strategies for Implantable Bioelectronics," *IEEE Rev. Biomed. Eng.*, vol. 10, no. c, pp. 136–161, 2017, doi: 10.1109/RBME.2017.2683520.
- [5] R. Das and H. Yoo, "A Multiband Antenna Associating Wireless Monitoring and Nonleaky Wireless Power Transfer System for Biomedical Implants," *IEEE Trans. Microw. Theory Tech.*, vol. 65, no. 7, pp. 2485–2495, 2017, doi: 10.1109/TMTT.2017.2647945.
- [6] R. Das, A. Basir, and H. Yoo, "A Metamaterial-Coupled Wireless Power Transfer System Based on Cubic High-Dielectric Resonators," *IEEE Trans. Ind. Electron.*, 2019, doi: 10.1109/TIE.2018.2879310.
- [7] S. A. A. Shah and H. Yoo, "Radiative Near-Field Wireless Power Transfer to Scalp-Implantable Biotelemetry Device," *IEEE Trans. Microw. Theory Tech.*, vol. 68, no. 7, 2020, doi: 10.1109/TMTT.2020.2985356.
- [8] F. J. Huang, C. M. Lee, C. L. Chang, L. K. Chen, T. C. Yo, and C. H. Luo, "Rectenna application of miniaturized implantable antenna design for triple-band biotelemetry communication," *IEEE Trans. Antennas Propag.*, vol. 59, no. 7, pp. 2646–2653, 2011, doi: 10.1109/TAP.2011.2152317.
- [9] A. D. Rush and P. R. Troyk, "A power and data link for a wireless-implanted neural recording system," *IEEE Trans. Biomed. Eng.*, vol. 59, no. 12, PART2, pp. 3255–3262, 2012, doi: 10.1109/TBME.2012.2214385.
- [10] C. Liu, Y. X. Guo, H. Sun, and S. Xiao, "Design and safety considerations of an implantable rectenna for far-field wireless power transfer," *IEEE Trans. Antennas Propag.*, vol. 62, no. 11, pp. 5798–5806, 2014, doi: 10.1109/TAP.2014.2352363.
- [11] R. Salama, S. Kharkovsky, R. Liyanapathirana, and U. Gunawardana, "Wireless power transmission in human tissue for nerve stimulation," vol. 10, pp. 670–675, 2016, doi: 10.1049/iet-map.2015.0285.
- [12] Z. Liu, Z. Zhong, and Y. X. Guo, "In Vivo High-Efficiency Wireless Power Transfer with Multisine Excitation," *IEEE Trans. Microw. Theory Tech.*, vol. 65, no. 9, pp. 3530–3540, 2017, doi: 10.1109/TMTT.2017.2681652.
- [13] M. Manoufali, K. Bialkowski, B. J. Mohammed, P. C. Mills, and A. Abbosh, "Near-field inductive-coupling link to power a three-dimensional millimeter-size antenna for brain implantable medical devices," *IEEE Trans. Biomed. Eng.*, vol. 65, no. 1, pp. 4–14, 2018, doi: 10.1109/TBME.2017.2778729.
- [14] A. Abdi and H. Aliakbarian, "A Miniaturized UHF-Band Rectenna for Power Transmission to Deep-Body Implantable Devices," *IEEE J. Transl. Eng. Heal. Med.*, vol. 7, no. May, pp. 1–11, 2019, doi: 10.1109/JTEHM.2019.2910102.
- [15] S. Bakogianni and S. Koulouridis, "A Dual-Band Implantable Rectenna for Wireless Data and Power Support at Sub-GHz Region," *IEEE Trans. Antennas Propag.*, vol. 67, no. 11, pp. 6800–6810, 2019, doi: 10.1109/TAP.2019.2927879.
- [16] A. Basir and H. Yoo, "Efficient Wireless Power Transfer System with a Miniaturized Quad-Band Implantable Antenna for Deep-Body Multitasking Implants," *IEEE Trans. Microw. Theory Tech.*, 2020, doi: 10.1109/TMTT.2020.2965938.
- [17] M. Wang *et al.*, "Broadband Implantable Antenna for Wireless Power Transfer in Cardiac Pacemaker Applications," *IEEE J. Electromagn. RF Microwaves Med. Biol.*, vol. 5, no. 1, pp. 2–8, 2021, doi: 10.1109/JERM.2020.2999205.
- [18] T. Shaw, G. Samanta, and D. Mitra, "Efficient Wireless Power Transfer System for Implantable Medical Devices Using Circular Polarized Antennas," *IEEE Trans. Antennas Propag.*, vol. 69, no. 7, pp. 4109–4122, 2021, doi: 10.1109/TAP.2020.3044636.
- [19] A. Iqbal, M. Al-Hasan, I. Ben Mabrouk, A. Basir, M. Nedil, and H. Yoo, "Biotelemetry and Wireless Powering of Biomedical Implants Using a Rectifier Integrated Self-Diplexing Implantable Antenna," *IEEE Trans. Microw. Theory Tech.*, vol. 69, no. 7, pp. 3438–3451, 2021, doi: 10.1109/TMTT.2021.3065560.
- [20] X. Yang *et al.*, "Wandering Pattern Sensing at S-Band," *IEEE J. Biomed. Heal. Informatics*, vol. 22, no. 6, pp. 1863–1870, 2018, doi: 10.1109/JBHI.2017.2787595.
- [21] X. Yang *et al.*, "Freezing of Gait Detection Considering Leaky Wave Cable," *IEEE Trans. Antennas Propag.*, vol. 67, no. 1, pp. 554–561, 2019, doi: 10.1109/TAP.2018.2878081.
- [22] J. Sarrazin, Y. Mahé, S. Avrillon, and S. Toutain, "Pattern reconfigurable cubic antenna," *IEEE Trans. Antennas Propag.*, 2009, doi: 10.1109/TAP.2008.2011221.

- [23] H. Sun and W. Geyi, "A New Rectenna with All-Polarization-Receiving Capability for Wireless Power Transmission," *IEEE Antennas Wirel. Propag. Lett.*, vol. 15, pp. 814–817, 2016, doi: 10.1109/LAWP.2015.2476345.
- [24] A. Khalifa *et al.*, "The Microbead: A Highly Miniaturized Wirelessly Powered Implantable Neural Stimulating System," *IEEE Trans. Biomed. Circuits Syst.*, vol. 12, no. 3, pp. 521–531, 2018, doi: 10.1109/TBCAS.2018.2802443.
- [25] C. Liu, Y. Zhang, and X. Liu, "Circularly Polarized Implantable Antenna for 915 MHz ISM-Band Far-Field Wireless Power Transmission," *IEEE Antennas Wirel. Propag. Lett.*, 2018, doi: 10.1109/LAWP.2018.2790418.
- [26] B. N. Getu and J. B. Andersen, "The MIMO cube - A compact MIMO antenna," *IEEE Trans. Wirel. Commun.*, vol. 4, no. 3, pp. 1136–1141, 2005, doi: 10.1109/TWC.2005.846997.
- [27] C. M. Kruesi, R. J. Vyas, and M. M. Tentzeris, "Design and development of a novel 3-D cubic antenna for wireless sensor networks (WSNs) and RFID applications," *IEEE Trans. Antennas Propag.*, vol. 57, no. 10 PART 2, pp. 3293–3299, 2009, doi: 10.1109/TAP.2009.2028672.
- [28] S. Chen and K. M. Luk, "A dual-mode wideband MIMO cube antenna with magneto-electric dipoles," *IEEE Trans. Antennas Propag.*, vol. 62, no. 12, pp. 5951–5959, 2014, doi: 10.1109/TAP.2014.2359492.
- [29] Y. Yang *et al.*, "A Circularly Polarized Rectenna Array Based on Substrate Integrated Waveguide Structure with Harmonic Suppression," *IEEE Antennas Wirel. Propag. Lett.*, vol. 17, no. 4, pp. 684–688, 2018, doi: 10.1109/LAWP.2018.2811860.
- [30] A. Kiourti, J. R. Costa, C. A. Fernandes, and K. S. Nikita, "A broadband implantable and a dual-band on-body repeater antenna: Design and transmission performance," *IEEE Trans. Antennas Propag.*, vol. 62, no. 6, pp. 2899–2908, 2014, doi: 10.1109/TAP.2014.2310749.
- [31] S. Alamri, A. Alamoudi, and R. Langley, "Gain enhancement of implanted antenna using lens and parasitic ring," vol. 52, no. 10, pp. 800–801, 2016, doi: 10.1049/el.2015.3371.
- [32] K. Zhang *et al.*, "A Conformal Differentially Fed Antenna for Ingestible Capsule System," *IEEE Trans. Antennas Propag.*, 2018, doi: 10.1109/TAP.2018.2804673.
- [33] S. A. A. Shah and H. Yoo, "Scalp-Implantable Antenna Systems for Intracranial Pressure Monitoring," *IEEE Trans. Antennas Propag.*, 2018, doi: 10.1109/TAP.2018.2801346.
- [34] V. Kaim, B. K. Kanaujia, and K. Rambabu, "Quadrilateral Spatial Diversity Circularly Polarized MIMO Cubic Implantable Antenna System for Biotelemetry," *IEEE Trans. Antennas Propag.*, 2020, doi: 10.1109/tap.2020.3016483.
- [35] V. Kaim, B. Kanaujia, S. Kumar, H. C. Choi, K. W. Kim, and K. Rambabu, "Electrically Small Circularly Polarized UWB Intraocular Antenna System for Retinal Prosthesis," *IEEE Trans. Biomed. Eng.*, 2022, doi: 10.1109/TBME.2022.3171842.
- [36] J. O. McSpadden, T. Yoo, and K. Chang, "Theoretical and experimental investigation of a rectenna element for microwave power transmission," *IEEE Trans. Microw. Theory Tech.*, 1992, doi: 10.1109/22.179902.
- [37] M. S. Islam, K. P. Esselle, D. Bull, and P. M. Pilowsky, "Converting a wireless biotelemetry system to an implantable system through antenna redesign," in *IEEE Transactions on Microwave Theory and Techniques*, 2014, vol. 62, no. 9, pp. 1890–1897, doi: 10.1109/TMTT.2014.2342665.
- [38] K. Bazaka and M. V. Jacob, "Implantable devices: Issues and challenges," *Electronics (Switzerland)*, vol. 2, no. 1, pp. 1–34, 2012, doi: 10.3390/electronics2010001.
- [39] R. Xu, J. Y. Li, J. Liu, S. G. Zhou, K. Wei, and Z. J. Xing, "A Simple Design of Compact Dual-Wideband Square Slot Antenna with Dual-Sense Circularly Polarized Radiation for WLAN/Wi-Fi Communications," *IEEE Trans. Antennas Propag.*, vol. 66, no. 9, pp. 4884–4889, 2018, doi: 10.1109/TAP.2018.2851671.
- [40] A. Ma and A. S. Y. Poon, "Midfield wireless power transfer for bioelectronics," *IEEE Circuits Syst. Mag.*, 2015, doi: 10.1109/MCAS.2015.2418999.
- [41] D. Andreuccetti, R. Fossi, and C. Petrucci, "An Internet resource for the calculation of the dielectric properties of body tissues in the frequency range 10 Hz - 100 GHz," *Website at niremf.ifac.cnr.it/tissprop/*, 1997. .
- [42] J. W. Massey and A. E. Yilmaz, "AustinMan and AustinWoman: High-fidelity, anatomical voxel models developed from the VHP color images," 2016, doi: 10.1109/EMBC.2016.7591444.
- [43] S. M. Asif, A. Iftikhar, B. D. Braaten, D. L. Ewert, and K. Maile, "A Wide-Band Tissue Numerical Model for Deeply Implantable Antennas for RF-Powered Leadless Pacemakers," *IEEE Access*, 2019, doi: 10.1109/ACCESS.2019.2902981.
- [44] A. T. Mobashsher and A. M. Abbosh, "Artificial human phantoms: Human proxy in testing microwave apparatuses that have electromagnetic interaction with the human body," *IEEE Microw. Mag.*, 2015, doi: 10.1109/MMM.2015.2419772.
- [45] A. La Gioia *et al.*, "Open-Ended Coaxial Probe Technique for Dielectric Measurement of Biological Tissues: Challenges and Common Practices," *Diagnostics*, vol. 8, no. 2, p. 40, 2018, doi: 10.3390/diagnostics8020040.
- [46] A. C. K. Mak, C. R. Rowell, and R. D. Murch, "Isolation enhancement between two closely packed antennas," *IEEE Trans. Antennas Propag.*, vol. 56, no. 11, pp. 3411–3419, 2008, doi: 10.1109/TAP.2008.2005460.
- [47] H. Wong, W. Lin, L. Huitema, and E. Arnaud, "Multi-Polarization Reconfigurable Antenna for Wireless Biomedical System," *IEEE Trans. Biomed. Circuits Syst.*, vol. 11, no. 3, pp. 652–660, 2017, doi: 10.1109/TBCAS.2016.2636872.
- [48] R. A. Bercich, D. R. Duffy, and P. P. Irazoqui, "Far-field RF powering of implantable devices: Safety considerations," *IEEE Trans. Biomed. Eng.*, vol. 60, no. 8, pp. 2107–2112, 2013, doi: 10.1109/TBME.2013.2246787.
- [49] F. Faisal and H. Yoo, "A miniaturized novel-shape dual-band antenna for implantable applications," *IEEE Trans. Antennas Propag.*, vol. 67, no. 2, pp. 774–783, Feb. 2019, doi: 10.1109/TAP.2018.2880046.